# Probing Cold Sintering-Regulated Interfaces and Integration of Polymer-in-Ceramic Solid-State Electrolytes

Bo Nie[1], and Hongtao Sun[1,2*]

*[1]The Harold & Inge Marcus Department of Industrial & Manufacturing Engineering, Pennsylvania State University, University Park, PA, USA. [2]Materials Research Institute (MRI), Pennsylvania State University, University Park, PA, USA*

## ABSTRACT

Solid-state batteries (SSBs) have recently been revived to increase energy density and eliminate safety concerns of current Li-ion batteries that use flammable liquid electrolytes. However, fabricating solid-state electrolytes (SSEs) faces many challenges, particularly the lack of effective methods to integrate reactive and sensitive solid ceramic conductors and address interfacial issues. To overcome these challenges, we introduce a cold sintering process (CSP) to integrate dissimilar conducting materials into polymer-in-ceramic (PIC) composite SSEs under external stress and mild heating conditions. Specifically, a NASICON phase $Li_{1.3}Al_{0.3}Ti_{1.7}(PO_4)_3$ (LATP)-based composite SSEs were co-sintered, resulting in well-distributed polymer-in-ionic liquid gel (PILG) along the ceramic boundaries. Using electrochemical impedance spectroscopy (EIS), we monitored real-time impedance during the CSP, revealing the effect of the transient liquid on boundary formation in the PIC composite. The cold sintering-regulated composite structure demonstrated excellent charge transport capabilities. For example, it achieved a room temperature ionic conductivity of $4.2\times10^{-4}$ S cm$^{-1}$ and was able to reversibly transport $Li^+$ for hundreds of hours. Additionally, the co-sintering of multi-layered Li metal SSBs (*e.g.*, $LiFePO_4$-PILG||LATP-

---

[*]Corresponding authors

*Email address*: hzs5373@psu.edu (H. Sun)

PILG|PILG||Li) reduced interface resistance, thereby exhibiting stable cycling.

**Keywords**: In-situ EIS; cold sintering; solid-state electrolyte; ionic conductivity, polymer-in-ceramic composites

## 1. Introduction

All-solid-state batteries (ASSBs) have attracted enormous attention for their high energy density and power safety (*1-3*). The efforts of developing highly conductive solid electrolytes in the last decades make groups of electrochemical stable solid-state electrolytes available for different operational scenarios (sulfides: ~ 1.7 – 2.2 V; oxides: ~0.05 – 3.0 V; nitrides: ~0.7 – 1.1 V; chlorides: ~0.6 – 4.3 V; v. s. $Li^+/Li$) (*4-6*). Among them, oxide ceramics have lithium metal stable voltage windows and outstanding bulk ionic conductivities (~$10^4$ – $10^3$ S $cm^{-1}$). Together with the solid electrolytes, ASSBs have various interfaces, such as the cathode-electrolyte, electrolyte-boundaries, anode-electrolyte, and additive-electrolyte interfaces, causing resistance to charge transport and deteriorating the battery performance (*7-9*).

To mitigate these challenges, thermodynamic interphases and artificial buffer layers have been developed to tailor these interfaces (*10*). For example, the ALD-coated $Al_2O_3$ buffer layers were created not only to address the non-wettability between the lithium metal and solid electrolytes but also to overcome the interfacial compatibility issue between the cathode and solid electrolytes (*11, 12*). In addition to the buffer layers, $Li_3BO_3$, $Li_2SiO_3$, and their derivatives have been used as the bonding component of the composite in the sintering process because of their low melting point and decent $Li^+$ conductivity (*13-15*). These sintering additives lower the sintering temperature as well as form a stable interface between the electrolyte and electrode. These surface amorphous films and intergranular films with self-limiting or equilibrium thickness can prewet interfacial phase and promote battery performance. However, the sintering additives involved in conventional sintering processes still require high temperatures (>

500 °C) and long lead time (i.e. a couple of hours) (*16, 17*). That is, a lack of efficient methodology to address these interfacial issues in a mild process condition. The cold sintering process (CSP), which was developed by Randall (*18*), is an alternative to obtain dense ceramics at low temperatures (< 300 °C). This disruptive technique is based on the combination of a high uniaxial pressure (~500 MPa), and the presence of the sintering aid, Transient Liquid Phase (TLP). In such a semi-open system, TLP drives the densification process through the non-equilibrium thermodynamic process (*19-22*). It mimics the pressure solution creep mechanism in the geographic densification process, where the heat and applied uniaxial pressure induce partial material dissolution into the transient solvent and further promote mass diffusion and precipitation throughout the densification process. It enables CSP to produce the inorganic solid-state electrolyte with a relative density of> 90% at low temperatures (*23-26*). Attributed to the low sintering temperature, CSP can co-sinter distinct materials and achieve pronounced interfacial properties for the composites. For example, co-sintering ceramics with polymers, inorganic salts, or carbonaceous materials. Specifically, incorporated in the ceramic matrix or laminated between the ceramic layers, the polymer additional phase can effectively ameliorate these interfacial barriers of the dense ceramic-polymer composites (*27-29*).

With this in said, cold sintering has been demonstrated to sinter the ceramic-based electrolyte and achieve good conductivity. One of the excellent ionic conductive materials, the NASICON structured electrolytes, $Li_{1.5}Al_{0.5}Ge_{1.5}(PO_4)_3$ (LAGP) (*30*) and $Li_{1.3}Al_{0.3}Ti_{1.7}(PO_4)_3$ (LATP) (*31*), have been sintered to highly dense composites by CSP. These designed multiphase ceramic composite, ceramic-lithium salt composite, and ceramic-polymer composite can achieve high ionic conductivities over $10^{-4}$ $S\cdot cm^{-1}$, such as $Bi_2O_3$-LATP (*32*), LAGP-LiTFSI (*26*), LAGP-(PVDF-HFP) (*33*), and LATP-PEO/LiTFSI (*34*). The versatile capability of integrating amorphous ceramic phases, oxide nanolayers, lithium salts, or polymers with the ceramic matrix enables CSP to outperform these conventional high-temperature sintering processes on interface tunability. Specifically, different from the oxide electrolytes' low elasticity and low surface energy, polymers are known to have good wettability and processability. The incorporation of an ionic conductive polymer phase into ceramic-based composite electrolytes can not only maintain high electrochemical stability and bulk conductivity but also serve to address multiple interfacial factors, such as the improvement of bonds between the electrolyte primary particles and the electrode-electrolyte contact. By introducing a polymer, the composite electrolyte can be formulated to high relative density and facilitate the integration of the composite electrolyte and the solid-state battery assembly, thereby improving overall cell efficiency and reducing losses during charge-discharge cycles.

Here we employ a low-temperature densification process, a cold sintering process, to integrate distinct materials (LATP ceramics and polymers) for a highly dense PIC solid-state electrolyte (Fig. 1). The interface-regulated composite microstructure and properties together with the fabrication process are well-studied. Specifically, an in-situ electrochemical impedance spectroscopy (EIS) was designed to monitor the interface formation and dynamic properties during CSP (Fig. 1b), facilitating the fundamental understanding for tailoring interfaces in ceramic-based SSEs. Therefore, the sintered LATP-PILG composite electrolyte presents a high ionic conductivity of $4.2\times10^{-4}$ S $cm^{-1}$ at ambient conditions. Benefiting from the interface-regulated process-structure-property correlation, Li symmetric cells with the PILG-coated LATP-PILG bulk electrolyte exhibited a long Li stripping-plating lifespan of 200 h at 0.1 mA $cm^{-2}$. Moreover, the co-sintered solid-state half-cell of $LiFePO_4$-PILG||LATP-PILG|PILG||Li showed dramatically depressed interfacial reactions and total resistance, thereby delivering excellent cycling stability at various current rates. For example, 0.03 % capacity decay per cycle at 0.1 C, 55 °C after 150 cycles from the half-cell.

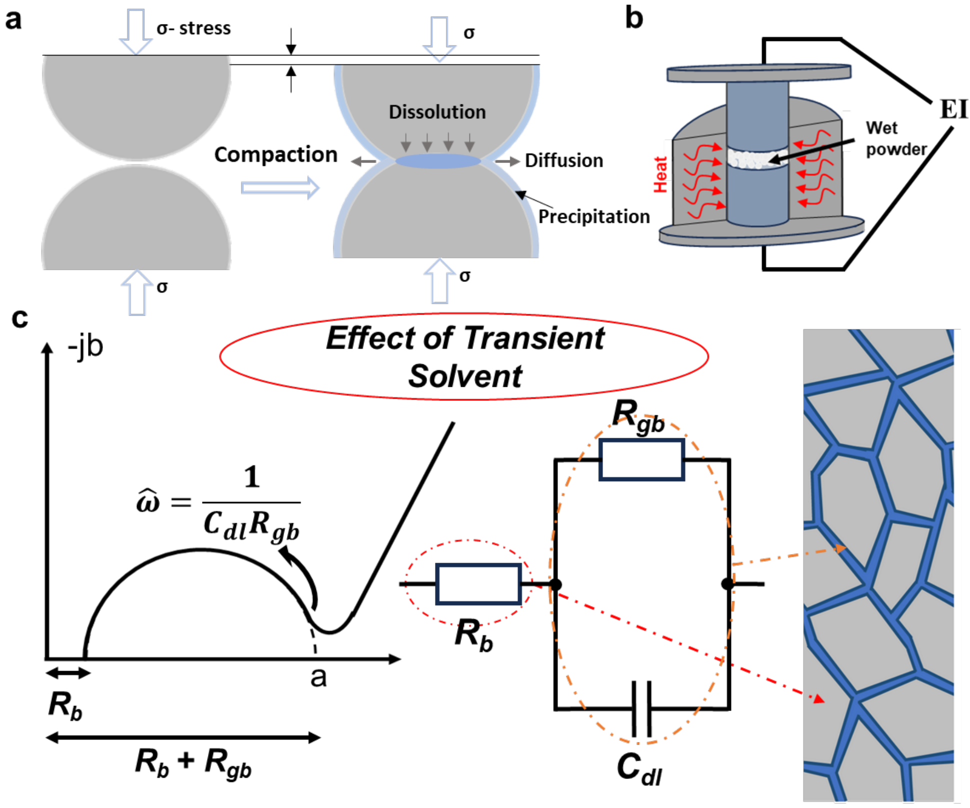

**Fig. 1. Illustration of the cold sintering process with in-situ EIS to monitor the microstructure evolution**. **a**, the schematic of the cold sintering process with the EIS measurement system; **b**, the sintering mechanism of the cold sintering process; **c**, the interpretation of the composite microstructure from the impedance results.

## 2. Results and discussion

### 2.1. Co-sintering inorganic and organic phases for highly ion-conductive solid-state electrolytes

Inspired by the geological consolidation process, CSP was designed with similar attributes to consolidate the materials or composites (*35*). The capillary forces and applied uniaxial pressure in combination with dissolution-based mass transport are presumably the densification mechanisms (Fig. 1a). It involves primary stages with dissolution, mass transport, and precipitation during the CSP. In these stages, due to the attributes of transient solvents, these critical stages were accelerated and enhanced to achieve the dense and robust bulk material, which makes co-sintering of ceramic and polymer possible at a low-temperature and short time. In this work, LATP powders were co-sintered with PILG gel (consisting of PVDF-HFP polymer and ionic liquid) to form the polymer-in-ceramic solid-state electrolyte (SSE) where the PILG diffuses across the LATP particles and modifies the boundary of the adjacent ceramic particles. Here the bulk pellets with different PILG contents were investigated for the ionic conductivity. The content of PILG was studied from 3 wt% to 12 wt%, the resulting Nyquist diagram shows that the 8 wt% of PILG in the composite solid-state electrolyte has the smallest resistance (Fig. 2a). In contrast, the derived pure LATP bulk electrolyte from the cold sintering process with DMF as transient solvent and the later high-temperature sintering process (900 °C, 5h) presented a large resistance from its impedance diagram (Fig. S1). According to the ionic diffusion characters at different testing frequencies (Fig. 2b), it is further analyzed by equivalent circuit fitting to interpret the boundary resistance of the bulk composite electrolyte. The LATP-PILG (8wt%) composite electrolyte shows the lowest grain boundary resistance ($R_{gb}$) of 161 Ω (Fig. 2c). The composite with lower or higher PILG amount resulted in a relatively higher $R_{gb}$. Furthermore, LATP-PILG (8 wt%) composite electrolyte was measured at different temperatures in Fig. 2d and Fig. S2. The conductivity of 0.42 and 2.19 mS cm$^{-1}$ were obtained at 30 and 80 °C, respectively. The value of active energy of the polymer-in-ceramic composite electrolyte was calculated from the Arrhenius equation (Eq.1) (*36*),

(Eq.1)

where $k_B$ is the Boltzmann constant and $A_{tot}$ is the preexponential factor. The $Ea$ is calculated as 0.135 eV, which is lower than most LATP ceramic electrolytes and LATP-based composite electrolytes and higher than gel electrolytes (Table S1), suggesting a low potential is needed to promote the transference of the Li$^+$ in the composite electrolyte.

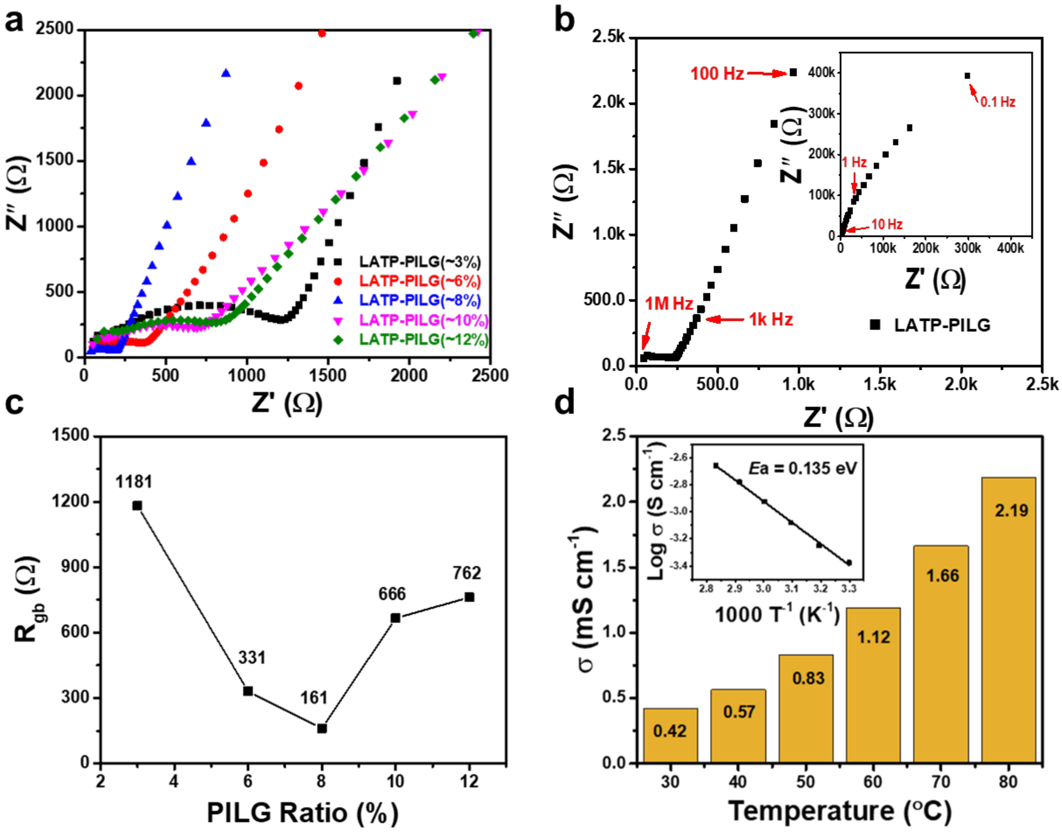

**Fig. 2. The ionic conductivity study of co-sintered LATP-PILG composite solid-state electrolytes**. **a**, the Nyquist results of the composite electrolyte with different PILG contents; **b**,**c**, the fitted grain boundary resistance from the resulting impedance diagram; **d**, the total ionic conductivity of the composite electrolyte at different test temperatures, the inset is the Arrhenius' plot and the mean activation energy ($E_a$).

The densified composite with a density of 2.41 g cm$^{-3}$ corresponds to a relative density of 86% with a porosity of 14%. Since the microstructure of the bulk composite can reveal the change after the sintering process, the morphology of the composite was studied. From the SEM images of sectioned dense electrolyte (Fig. 3a and 3b), the PILG was presented as the interparticle phase which appears as a coating on the surface of the particles. Moreover, it can be observed that the PILG phase is uniformly distributed across the view of the particles, indicating effective diffusion during the cold sintering process. The high-resolution image and corresponding elementary mapping in Fig. 3c and 3d confirm the distribution of the PILG phase and homogeneously dispersed inside the bulk electrolyte. From the X-ray diffraction spectra in Fig. 3e, the composite shows a pattern of LATP pattern (JCPDF card no. 00-35-0754) (*37*), meaning that the co-sintering at a low temperature of 150 ˚C does not change the crystalline structure of LATP. In addition, the two weight loss stage TGA profile of the composite electrolyte with optimized PILG content confirms a polymer phase content of ~8 wt%, including ~3.4 wt% of encapsulated IL, ~4.7 wt% of the uncomplexed polymer phase PVDF-HFP, and a small amount of the residual solvents (acetone or DMF) or the moisture adsorbed.

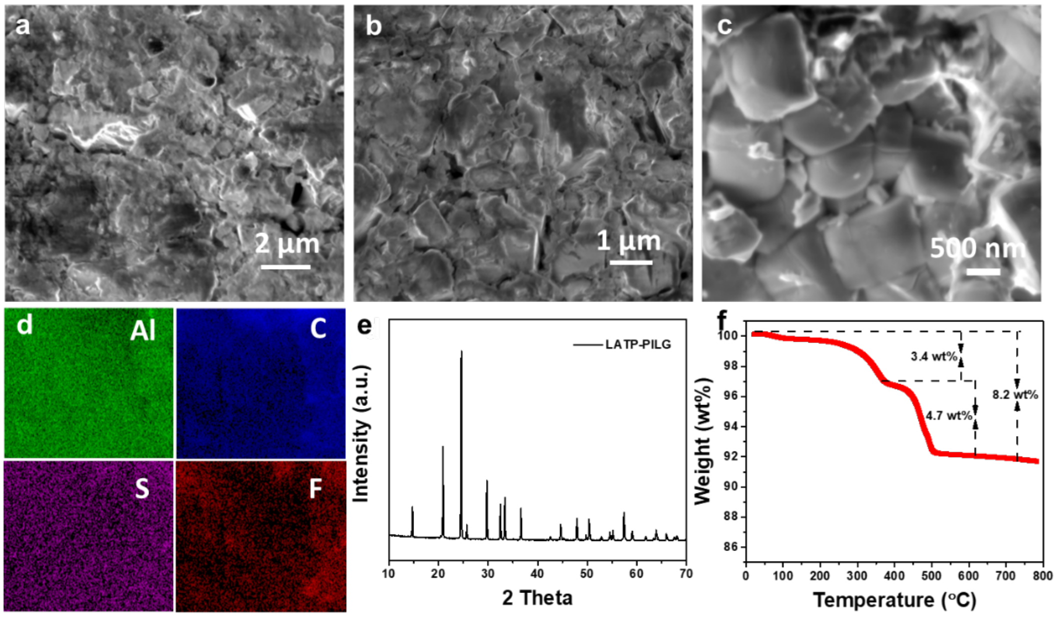

**Fig. 3.** The microstructure study of LATP-PILG composite solid-state electrolytes. **a**,**b**, the SEM images at the cross-sectional view of the composite electrolyte with optimized PILG content; **c**, the high-resolution image of the LATP particles and PILG phase; **d**, the EDS mapping of different elements from the composite; **e**, the X-ray diffraction pattern of the sintered LATP-PILG composite; **f**, the TGA profile of the composite electrolyte.

## 2.2. In situ probing the cold sintering-enabled densification of PIC composite SSE

The PIC composite SSE consisting of a LATP ceramic phase and a PILG polymer phase were sintered by introducing an organic liquid (DMF) as the transient liquid phase (TLP). To investigate the properties of the electrolytes and the effect of the transient solvent during the process, the in-situ EIS system was designed for the cold sintering process. The experimental setup was adapted as presented in Fig. 1b. Electrodes were connected on the external surface of both top and bottom punches, and a boron nitride (BN) sleeve was placed between the plungers and inner die surface to insulate from the outer metals. EIS measurements were recorded throughout the heating period, dwell duration, and cooling period of the cold sintering process. With the assistance of the equivalent circuit (*38*), the resulting impedance diagram can be interpreted as the microstructure evolution of the composite sintering process (Fig. 1c). The effect of transient solvent on the sintering system could be examined through this interpretation process.

In this work, the processes with and without introducing TLP wa studied to obtain the LATP-PILG composite solid-state electrolytes. During the CSP, the EIS was measured at specific temperatures and time stages as described in Fig. 4a. In the heating period, 4 impedance diagrams were compared at the temperature points of 30, 60, 90, and 120 °C. 5 diagrams were recorded in the dwell duration at 150 °C for every 15min. The impedance was measured at the same temperature points during the cooling as those recorded in the heating period. Throughout the process, the Nyquist plots show a decreasing 1st semi-circle and an increasing 1st semi-circle at the elevating temperatures and cooling temperatures, respectively. The semi-circles at lower temperatures suggest a dominant resistance of the boundaries, noting that the 2nd semi-circles were not complete due to the narrow frequency range. At the temperature of 150 °C, the 1st semi-circle disappears, showing that the boundary turns conductive and results in a conductive pathway through the sample. Based on the brick-layer model (*39*), two R-CPE units are connected in series as the equivalent circuit to fit the resistance of the composite electrolyte (Fig. 4a). The R-CPE for the 1st semi-circle represents the contribution of the grains and grain boundaries.

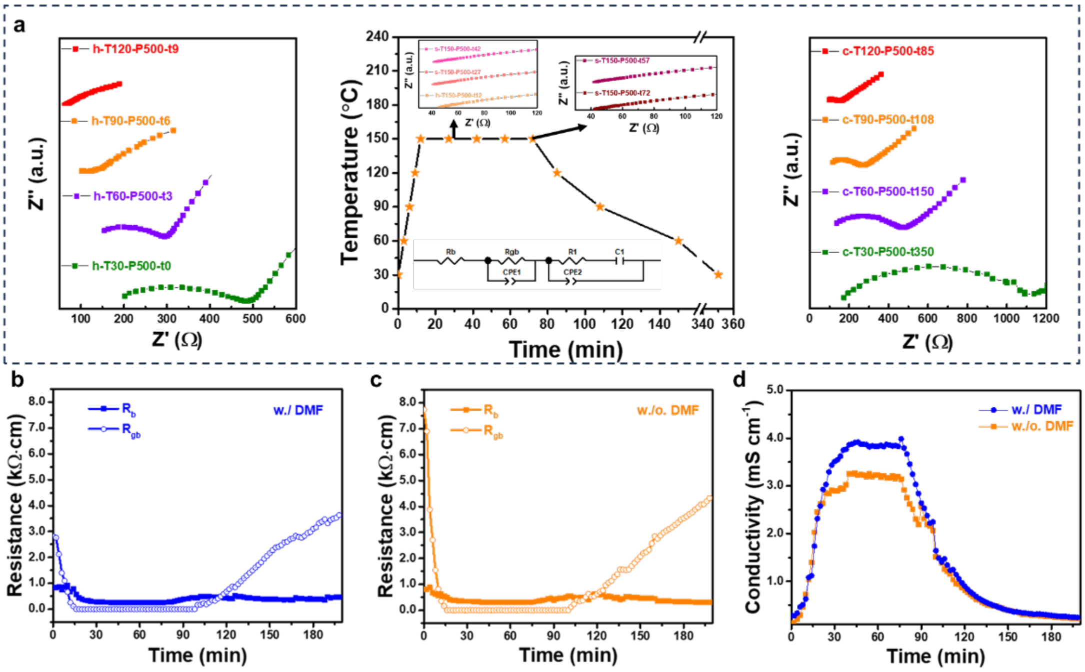

**Fig. 4.** In-situ EIS study of the transient solvent in the cold sintering process**. a**, the impedance diagram in the heating, dwell, and cooling periods of the cold sintering process, the label, h-T30-P500-t0, represents a heating process at the temperature of 30 °C, pressure of 500 MPa, and the time of 0 min; **b, c**, the resistance profiles of the sintering process with or without transient solvent (DMF), respectively; **d**, the evolution of the ionic conductivity during the process for the condition studied.

The fitted bulk resistance ($R_b$) and grain boundary resistance ($R_{gb}$) were plotted in Fig. 4b and 4c for the process with or without DMF solvent with more data points, respectively. Due to the temperature-dependent conductivity behavior of the grain and grain boundary, the resistance profiles of both two processes decrease with increasing temperatures. However, $R_{gb}$ shows a higher resistance change rate with time, indicating a dramatic evolution of the grain boundary, where the voids or gaps were occupied by the PILG phase. In the dwell period, the resistance shows an obvious change in the first 15 min and stays almost the same during the rest of the dwell stages. That is, after the 60-minute dwell time at 150 °C, the stabilized resistance confirms that the TLP has been vaporized and that the cold sintering is accomplished. However, during the cooling process, the derived $R_{gb}$ values at the corresponding temperatures are relatively higher than the heating process. It can be explained by the transition of a liquid phase-filled grain boundary to a quasi-phase-filled grain boundary due to the escaped transient solvent. The two processes show a $R_{gb}$ dominated resistance behavior throughout the sintering process. The fitted resistance data was employed to calculate the total ionic conductivity $\sigma_{tot}$ of the cold-sintered composite electrolytes. The evolution of $\sigma_{tot}$ for different processes was compared in Fig. 4d. As it can be seen, the ionic conductivity increases by introducing TLP, suggesting the enhanced dissolution and precipitation of the PILG on grain boundaries, thus increasing the sinterization degree of the pellet, which is supported by the CSP mechanism (pressure solution creep).

## 2.3. Assessment of electrochemical performance for ASSBs

The derived LATP-PILG composite electrolytes from the cold sintering process with DMF and the process without DMF (2.41 v.s. 2.38 g cm$^{-3}$) were further tested in a coin cell for a regular frequency range of EIS measurement (Fig. 5a). LATP-PILG composite from the DMF incorporated process shows a much lower resistance with the $R_{gb}$ of 161 Ω which is much lower than the composite without DMF involved ($R_{gb}$: 676 Ω). When coated with a thin layer of PILG on both sides to assemble the symmetric cell with Li foils, the stripping and plating behavior of the two electrolytes was compared in Fig. 5b. Across the current density of 0.05 to 0.4 mA cm$^{-2}$, the cold sintered LATP-PILG with DMF shows a lower overpotential and stable stripping and plating behavior, which confirms with the previous grain boundary resistance comparison. The LATP-PILG composite can also be stripped and plated for a prolonged cycling test (Fig. 5c). Furthermore, the PILG-coated LATP-PILG composite electrolyte shows no obvious current at the potential window of 2.0 – 5.5 V in the linear sweep voltammetry test and a higher stability than the pure PILG gel electrolyte (Fig. 5d).

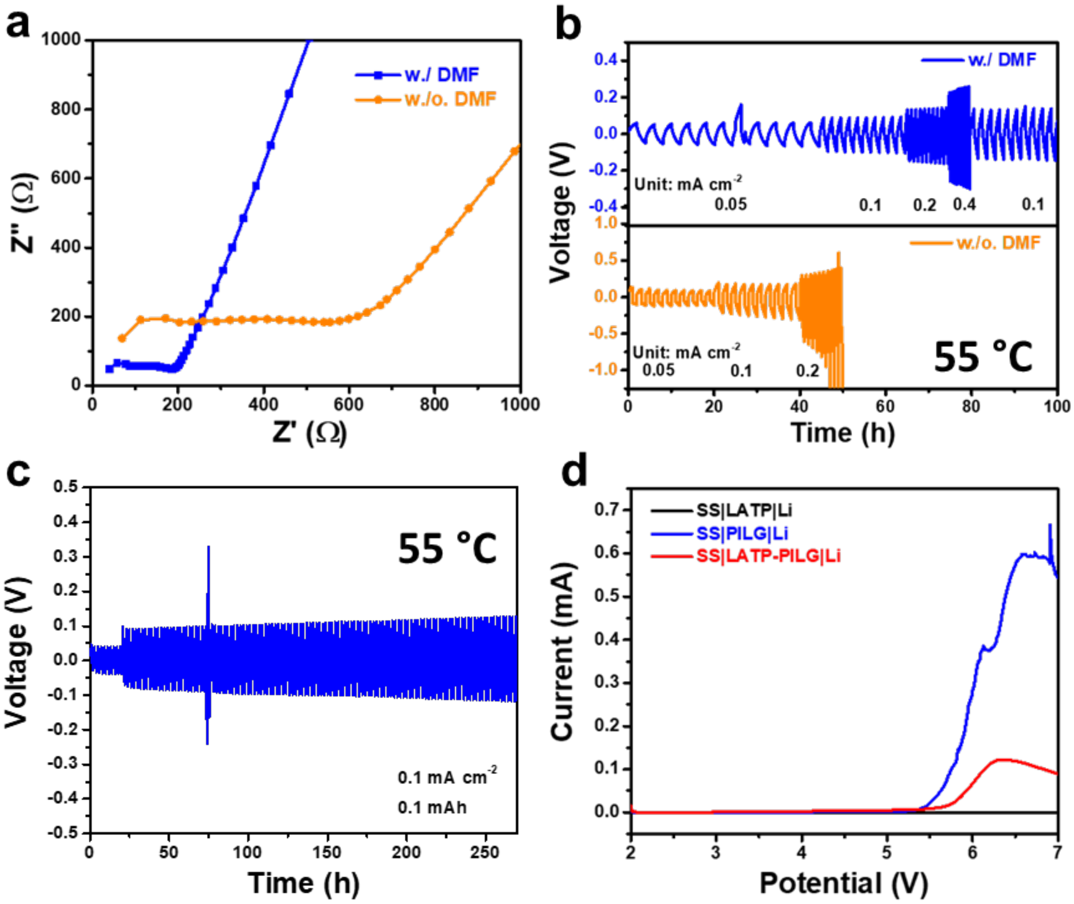

**Fig. 5.** The lithium stripping and plating behavior study of the cold-sintered composite electrolytes. **a**, **b**, the Nyquist plot (room temperature) and the stripping and plating behavior (55 °C) at different current densities of the LATP-PILG composite electrolytes w./ DMF or w./o. DMF; **c,** the prolonged DC cycling of the cold sintered LATP-PILG composite electrolyte at 0.1 mA cm$^{-2}$ and capacity of 0.1 mAh; **d**, the electrochemical stability of the derived LATP-PILG composite electrolyte.

To further evaluate the electrochemical performance of LATP-PILG composite electrolytes, solid-state half cells were assembled using co-sintered LFP-PILG|LATP-PILG bulk assembly and Li metal. The co-sintered LFP-PILG|LATP-PILG pellets enable an improved contact between the cathode and electrolyte (Fig. 6a), where part of the PILG diffused to the other components and bridged the cathode and electrolyte together. The side facing the Li metal was coated by a thin layer of PILG to ensure good Li$^+$ transport at the LATP-PILG and Li metal interface. Fig. 6b shows the charge-discharge curve of the half-cell at a current density of 0.05 C and temperature of 55 °C.

The charging and discharge plateaus are flat with a voltage gap of 0.13 V due to the overpotential. The rate performance of LFP-PILG||LATP-PILG|PILG||Li cell at 55 ˚C shows the discharge capacity decreased gently as the current rate rose. Discharge capacities of 168.8, 164.3, 133.7, 88.8, and 61.6 were obtained at the current rates of 0.05, 0.1, 0.2, 0.5, and 1C, respectively. When the current rate returned to 0.1 C, the capacity recovered to 160 mAh $g^{-1}$. In addition, the half-cell exhibited a high and stable Coulombic efficiency of 99% at various current rates. Moreover, the cells were further cycled over 170 cycles and retained the capacity of 152.4 mAh $g^{-1}$ (Fig. 6d), corresponding to a capacity retention of 95.3 % (i.e., 0.03 % capacity decay per cycle).

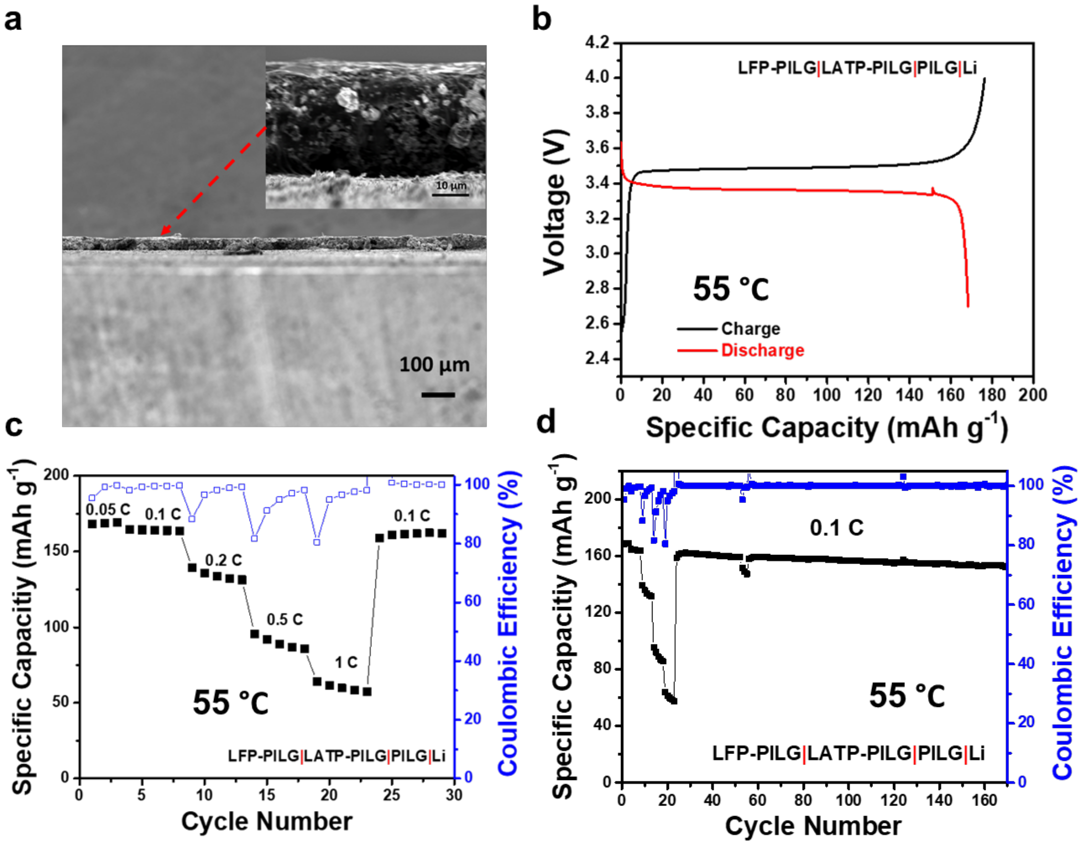

**Fig. 6.** The electrochemical performance of the half-cell and the full-cell assembled with LATP-PILG composite electrolytes. a, the SEM of the co-sintered LFP-PILG cathode and LATP-PILG composite electrolyte; **b**, the charge-discharge curve of the LFP-PILG||LATP-PILG|PILG||Li half-cell at 0.05C and 55 ˚C; **c**, **d**, the rate performance and the prolonged cycling at 0.1 C of the half-cell at 55 ˚C.

# 3. Conclusion

In summary, we demonstrate the in-situ EIS can effectively monitor the cold sintering process for LATP-PILG composite electrolyte production. The obtained LATP-PILG electrolyte exhibits good ionic conductivity and potential for high-performance energy storage in solid-state batteries. In-situ EIS throughout the cold sintering process unveiled the resistance evolution during the heating, dwell, and cooling period of the sintering process, which provided insight into the effective mass diffusion and precipitation along the grain boundary by introducing the transient solvent. The cold-sintered LATP-PILG composite electrolytes were able to stably strip and plate $Li^+$ at various current rates. The ability of co-sinter LATP-PILG and electrodes together addressed the interfacial challenges of solid-state electrolytes and enabled an effective charge transport pathway between the cathode and anode. The resulting half-cell delivers a capacity of 152.4 mAh $g^{-1}$ after 150 cycles at 0.1 C and the rate cycling. Therefore, this research provides a new technique for the obtention of highly conductive LATP-based hybrid electrolytes from the Polymer-In-Ceramics perspective.

# 4. Material and Methods

**4.1. Preparation of Polymer Solution (PILG).** 1-Ethyl-3-methylimidazolium bis(trifluoromethanesulfonyl)imide (EMIM-TFSI, Sigma) was dehydrated with the molecular sieves for 48h. Poly(vinylidene fluoride-co-hexafluoropropylene) (PVDF-HFP, Mw ~ 455,000, Sigma), EMIM-TFSI, and Lithium bis(trifluoromethane)sulfonimide (LiTFSI, Sigma) were dissolved in acetone (anhydrous, ≥99.8%, Sigma) in a mass ratio of 0.3 : 0.55 : 0.15. The stock solution was stored inside the glovebox.

**4.2. Fabrication of LATP-PILG Composite Electrolyte.** LATP powders (MSE Supplies Inc.) and PILG were well-mixed by the Thicky Centrifugation Mixer at 2000 rpm for 20 min. The ratio between LATP and PILG varied from 0.97: 0.03 to 0.85: 0.15. The mixed powder was mixed with a small amount of Dimethylformamide (DMF, anhydrous, Sigma) by the mortar and pestle. Then, the material was transferred into the cold sintering die with two aluminum foils (Al) attached between the material and the upper/ lower die. The bulk electrolyte pellet was sintered at a low temperature of 150 ˚C for 60 min with a heating rate of 10 ˚C min$^{-1}$.

**4.4. Preparation of Slurry Electrodes.** The electrodes were prepared by a slurry coating process. LFP-PILG or NMC811-PILG cathodes were prepared by mixing 80 wt % $LiFePO_4$ (LFP, MTI Co., Ltd.) or $LiNi_{0.8}Co_{0.1}Mn_{0.1}O_2$ (NMC, MTI Co., Ltd.), 10 wt % super P black (MTI Co., Ltd.), and 10 wt % PILG dissolved in DMF. The above slurry was coated on Al and Copper foils, respectively. The electrodes were dried at 120 ˚C under vacuum for 12 h to remove the solvent and then punched into a disk and pressed. The mass loading of the active materials is 2.1- 2.5 mg cm$^{-2}$.

**4.5. In-situ Electrochemical Impedance Spectroscopy (EIS) monitoring.** The cold sintering die was modified with a boron nitride (BN) sleeve and two leads welded at the upper/lower die terminals. In-situ EIS (Ametek, Princeton Applied Research, Versa STAT 4) measurements were performed with a sinusoidal signal in a frequency range from 100 kHz to 100 Hz at an amplitude of 100 mV at specific temperatures throughout the cold sintering process.

**4.6. Material Characterizations.** The morphological and structural characteristics were conducted by scanning electron microscopy (SEM, Thermoscientific Verios G4) and X-ray diffraction (XRD) (Panalytical Empyrean 3 Powder Diffractometer). Thermogravimetric analysis (TGA, Discovery TGA-MS) was conducted in an air atmosphere from room temperature to 800 ˚C at a heating rate of 10 ˚C min$^{-1}$.

**4.6. Electrochemical Measurements.** The ionic conductivity of the prepared LATP-PILG composite solid electrolytes between two stainless steel (SS) blocking electrodes was conducted by the EIS at open circuit potential with a sinusoidal signal in a frequency range from 100 kHz to 10 mHz at an amplitude of 10 mV. To assemble symmetric cells, the Al-peeled LATP-PILG electrolyte pellets were coated with a thin layer of PILG by drop casting 40 µL of PILG solution on both sides and then being vacuum dried at 120 ˚C for 3h. The LSV test was conducted by assembling the coated electrode between a stainless-steel disk and Li metal in a CR 2023-coin cell and then scanned from 2 to 7 V with a scan rate of 20 mV min$^{-1}$ (Versa STAT 4). The coated electrolyte was sandwiched between two thin Li disks (100 µm) to form a symmetric cell and evaluated in a DC cycling test (Landt Instrument). The current densities from 0.05 mA cm$^{-2}$ to 0.4 mA cm$^{-2}$ were applied for 1hr during the repeated stripping and plating process. To assemble the half-cell or full-cell, the LFP-PILG or NMC811-PILG electrodes or both electrodes were co-sintered with the LATP-PILG composite during the cold sintering process. The other side of the pellet for half-cell was further coated with a thin layer of PILG by drop casting and vacuum drying. By stacking it with a 100 µm thick Li disk in a coin cell, the LFP-PILG|LATP-PILG|Li half-cells were tested at various rates of 0.05-1.0 C and a voltage window of 2.7-4.0 V.

## Declaration of Competing interests

The authors declare no competing financial interests.

## CrediT authorship contribution statement

**Bo Nie**: Conceptualization, Methodology, Formal analysis, Inversitigation, Writing – original draft, Visualization, Writing – review & editing. **Hongtao Sun**: Conceptualization, Writing – review & editing, Supervision, Resources, Project administration.

## Acknowledgements

HS acknowledges financial support from the Pennsylvania State University start-up fund.

## Appendix. Supporting materials

Supplementary information is available in the online version of the paper.

# References

1. Q. Zhao, S. Stalin, C.-Z. Zhao, L. A. Archer, Designing solid-state electrolytes for safe, energy-dense batteries. *Nature Reviews Materials* **5**, 229-252 (2020).
2. M. J. Wang, E. Kazyak, N. P. Dasgupta, J. Sakamoto, Transitioning solid-state batteries from lab to market: Linking electro-chemo-mechanics with practical considerations. *Joule* **5**, 1371-1390 (2021).
3. S. Randau *et al.*, Benchmarking the performance of all-solid-state lithium batteries. *Nature Energy* **5**, 259-270 (2020).
4. M. Balaish *et al.*, Processing thin but robust electrolytes for solid-state batteries. *Nature Energy* **6**, 227-239 (2021).
5. W. Y. Liu *et al.*, Designing Polymer-in-Salt Electrolyte and Fully Infiltrated 3D Electrode for Integrated Solid-State Lithium Batteries. *ANGEWANDTE CHEMIE-INTERNATIONAL EDITION* **60**, 12931-12940 (2021).
6. R. X. Lv *et al.*, Preparing Two-Dimensional Ordered Li<sub>0.33</sub>La<sub>0.557</sub>TiO<sub>3</sub> Crystal in Interlayer Channel of Thin Laminar Inorganic Solid-State Electrolyte towards Ultrafast Li<SUP>+</SUP> Transfer. *ANGEWANDTE CHEMIE-INTERNATIONAL EDITION* **61**, (2022).
7. A. Banerjee, X. Wang, C. Fang, E. A. Wu, Y. S. Meng, Interfaces and Interphases in All-Solid-State Batteries with Inorganic Solid Electrolytes. *Chemical Reviews* **120**, 6878-6933 (2020).
8. B. Zahiri *et al.*, Revealing the role of the cathode–electrolyte interface on solid-state batteries. *Nature Materials* **20**, 1392-1400 (2021).
9. Y. Xiao *et al.*, Understanding interface stability in solid-state batteries. *Nature Reviews Materials* **5**, 105-126 (2020).
10. M. J. Du, K. M. Liao, Q. Lu, Z. P. Shao, Recent advances in the interface engineering of solid-state Li-ion batteries with artificial buffer layers: challenges, materials, construction, and characterization. *ENERGY & ENVIRONMENTAL SCIENCE* **12**, 1780-1804 (2019).
11. Y. L. Liu *et al.*, Stabilizing the Interface of NASICON Solid Electrolyte against Li Metal with Atomic Layer Deposition. *ACS APPLIED MATERIALS & INTERFACES* **10**, 31240-31248 (2018).
12. X. G. Han *et al.*, Negating interfacial impedance in garnet-based solid-state Li metal batteries. *NATURE MATERIALS* **16**, 572-+ (2017).
13. T. Liu *et al.*, Achieving high capacity in bulk-type solid-state lithium ion battery based on Li<sub>6.75</sub>La<sub>3</sub>Zr<sub>1.75</sub>Ta<sub>0.25</sub>O<sub>12</sub> electrolyte: Interfacial resistance. *JOURNAL OF POWER SOURCES* **324**, 349-357 (2016).
14. F. D. Han *et al.*, Interphase Engineering Enabled All-Ceramic Lithium Battery. *JOULE* **2**, 497-508 (2018).
15. G. V. Alexander, N. C. Rosero-Navarro, A. Miura, K. Tadanaga, R. Murugan, Electrochemical performance of a garnet solid electrolyte based lithium metal battery with interface modification. *JOURNAL OF MATERIALS CHEMISTRY A* **6**, 21018-21028 (2018).
16. B. Nie *et al.*, Cold sintering-enabled interface engineering of composites for solid-state

batteries. *FRONTIERS IN ENERGY RESEARCH* **11**, (2023).

17. Y. L. Liu *et al.*, Development of the cold sintering process and its application in solid-state lithium batteries. *JOURNAL OF POWER SOURCES* **393**, 193-203 (2018).
18. H. Z. Guo, A. Baker, J. Guo, C. A. Randall, Protocol for Ultralow-Temperature Ceramic Sintering: An Integration of Nanotechnology and the Cold Sintering Process. *ACS NANO* **10**, 10606-10614 (2016).
19. S. A. Pervez *et al.*, Overcoming the Interfacial Limitations Imposed by the Solid-Solid Interface in Solid-State Batteries Using Ionic Liquid-Based Interlayers. *SMALL* **16**, (2020).
20. J. Z. Zhang *et al.*, Effect of LiOH solution additives on ionic conductivity of Li<sub>6.25</sub>Al<sub>0.25</sub>La<sub>3</sub>Zr<sub>2</sub>O<sub>12</sub> electrolytes prepared by cold sintering. *JOURNAL OF MATERIALS SCIENCE-MATERIALS IN ELECTRONICS* **33**, 19187-19194 (2022).
21. H. Z. Guo, A. Baker, J. Guo, C. A. Randall, Cold Sintering Process: A Novel Technique for Low-Temperature Ceramic Processing of Ferroelectrics. *JOURNAL OF THE AMERICAN CERAMIC SOCIETY* **99**, 3489-3507 (2016).
22. S. Kim, Y. Gim, W. Lee, Thermally Stable Ceramic-Salt Electrolytes for Li Metal Batteries Produced from Cold Sintering Using DMF/Water Mixture Solvents. *NANOMATERIALS* **13**, (2023).
23. H. Cai *et al.*, Microstructure and ionic conductivities of NASICON-type Li1.3Al0.3Ti1.7(PO4)3 solid electrolytes produced by cold sintering assisted process. *Journal of Alloys and Compounds* **939**, 168702 (2023).
24. A. Mormeneo-Segarra, S. Ferrer-Nicomedes, N. Vicente-Agut, A. Barba-Juan, In operando characterization of the ionic conductivity dependence on liquid transient phase and microstructure of cold-sintered Bi2O3-doped Li1.3Al0.3Ti1.7(PO4)3 solid-state electrolyte. *Ceramics International* **49**, 36497-36506 (2023).
25. P. Jiang *et al.*, Solid-state Li metal battery enabled by cold sintering at 120 °C. *MATERIALS TODAY PHYSICS* **20**, (2021).
26. W. Lee *et al.*, Ceramic-Salt Composite Electrolytes from Cold Sintering. *ADVANCED FUNCTIONAL MATERIALS* **29**, (2019).
27. J. Guo *et al.*, Cold Sintering Process of Composites: Bridging the Processing Temperature Gap of Ceramic and Polymer Materials. *ADVANCED FUNCTIONAL MATERIALS* **26**, 7115-7121 (2016).
28. S. Vinoth, S.-F. Wang, Cold Sintering Process for a BaTiO3/Poly(vinylidene difluoride) Ceramic–Polymer Composite: Evaluation of the Structural and Microwave Dielectric Properties. *Inorganic Chemistry* **62**, 8326-8333 (2023).
29. S. Dursun, K. Tsuji, S. H. Bang, A. Ndayishimiye, C. A. Randall, A Route towards Fabrication of Functional Ceramic/Polymer Nanocomposite Devices Using the Cold Sintering Process. *ACS Applied Electronic Materials* **2**, 1917-1924 (2020).
30. K. Takashima, Y. Iwazaki, C. A. Randall, Cold sintering for Li<sub>1.5</sub>Al<sub>0.5</sub>Ge<sub>1.5</sub>(PO<sub>4</sub>)<sub>3</sub> using LiNO<sub>3</sub>-LiOH as a transient solvent. *JAPANESE JOURNAL OF APPLIED PHYSICS* **60**, (2021).
31. Y. L. Liu *et al.*, Insight into the Microstructure and Ionic Conductivity of Cold Sintered NASICON Solid Electrolyte for Solid-State Batteries. *ACS APPLIED MATERIALS &*

*INTERFACES* **11**, 27890-27896 (2019).

32. A. Mormeneo-Segarra *et al.*, Using in operando impedance spectroscopy technique to unravel the sintering process evolution of Bi2O3:LATP cold-sintered solid electrolyte. *Solid State Ionics* **406**, 116482 (2024).
33. S. S. Berbano, J. Guo, H. Z. Guo, M. T. Lanagan, C. A. Randall, Cold sintering process of Li<sub>1.5</sub>Al<sub>0.5</sub>Ge<sub>1.5</sub>(PO<sub>4</sub>)<sub>3</sub> solid electrolyte. *JOURNAL OF THE AMERICAN CERAMIC SOCIETY* **100**, 2123-2135 (2017).
34. S. Ferrer-Nicomedes, A. Mormeneo-Segarra, N. Vicente-Agut, A. Barba-Juan, Introducing an ionic conductive matrix to the cold-sintered Li<sub>1.3</sub>Al<sub>0.3</sub>Ti<sub>1.7</sub>(PO<sub>4</sub>)<sub>3</sub>-based composite solid electrolyte to enhance the electrical properties. *JOURNAL OF POWER SOURCES* **581**, (2023).
35. E. Gundersen, F. Renard, D. K. Dysthe, K. Bjorlykke, B. Jamtveit, Coupling between pressure solution creep and diffusive mass transport in porous rocks. *JOURNAL OF GEOPHYSICAL RESEARCH-SOLID EARTH* **107**, (2002).
36. M. Petrowsky, R. Frech, Temperature Dependence of Ion Transport: The Compensated Arrhenius Equation. *The Journal of Physical Chemistry B* **113**, 5996-6000 (2009).
37. R. DeWees, H. Wang, Synthesis and Properties of NaSICON-type LATP and LAGP Solid Electrolytes. *ChemSusChem* **12**, 3713-3725 (2019).
38. T. H. de Beauvoir, P. L. Taberna, P. Simon, C. Estournes, Cold Sintering Process characterization by<i> in</i><i> operando</i> electrochemical impedance spectroscopy. *JOURNAL OF THE EUROPEAN CERAMIC SOCIETY* **42**, 5747-5755 (2022).
39. S. Uhlenbruck, A Physical Derivation of the Capacitive Brick Layer Model in Polycrystalline Ceramics from Fundamental Electrodynamic Equations. *Journal of The Electrochemical Society* **169**, 106509 (2022).